Observation of magnetic diffusion in the Earth's outer core from Magsat, Ørsted, and CHAMP data

JOURNAL OF GEOPHYSICAL RESEARCH, VOL. 115, B05105, doi:10.1029/2009JB006994, 2010

Observation of magnetic diffusion in the Earth's outer core from Magsat, Ørsted, and CHAMP data

A. Chulliat[1] and N. Olsen[2]

Received 22 September 2009; revised 23 December 2009; accepted 6 January 2010; published 28 May 2010.

[1] The frozen flux assumption consists in neglecting magnetic diffusion in the core. It has been widely used to compute core flows from geomagnetic observations. Here we investigate the validity of this assumption over the time interval 1980–2005, using high-precision magnetic data from the Magsat, Ørsted, and CHAMP satellites. A detectable change of magnetic fluxes through patches delimited by curves of zero radial magnetic field at the core-mantle boundary is associated with a failure of the frozen flux assumption. For each epoch (1980 and 2005), we calculate spatially regularized models of the core field which we use to investigate the change of reversed magnetic flux at the core surface. The largest and most robust change of reversed flux is observed for two patches: one located under St. Helena Island (near 20°S, 15°E); the other, much larger, is located under the South Atlantic Ocean. We next calculate frozen-flux-constrained field models (i.e., pairs of models for epoch 1980 and 2005 having the same flux through patches delimited by curves of zero radial magnetic field), using a penalty method. We find that the frozen flux constraint does not lead to any significant increase of the global misfit. However, applying the constraint leads to a detectable increase of the scalar residuals at satellite altitude in the region of St. Helena, strongly suggesting a local failure of the frozen flux assumption. The observed flux expulsion within the St. Helena patch could result from the formation of a pair of "core spots," as predicted by numerical simulations of the geodynamo.

Citation: Chulliat, A., and N. Olsen (2010), Observation of magnetic diffusion in the Earth's outer core from Magsat, Ørsted, and CHAMP data, *J. Geophys. Res.*, *115*, B05105, doi:10.1029/2009JB006994.

1. Introduction

[2] The main part of the Earth's magnetic field is generated by convection flows in the liquid, electrically conducting outer core. This process, known as the geodynamo, involves an overall balance between field generation and its destruction by magnetic diffusion, due to the finite electrical conductivity of the core. This can be seen in the equation governing the time evolution of the core magnetic field **B** [e.g., *Gubbins and Roberts*, 1987]:

$$\frac{\partial \mathbf{B}}{\partial t} = \nabla \times (\mathbf{u} \times \mathbf{B}) + \eta \nabla^2 \mathbf{B} \ , \tag{1}$$

where **u** is the flow velocity and η the magnetic diffusivity in the core (defined as $\eta = 1/\mu_0\sigma$, where σ is the electrical conductivity in the core and μ_0 the vacuum permeability). The diffusive term (second of the right-hand side) counterbalances the field generation (first term of the right-hand side), and thus prevents the magnetic field to grow limitless.

[3] Although an essential ingredient of the geodynamo, magnetic diffusion is often neglected on timescales of decades to centuries. The reasoning behind this so-called *frozen flux* (FF) assumption [*Roberts and Scott*, 1965] is usually based on a simple scaling of the diffusion term. Taking $\eta = 2$ m^2/s [*Braginsky and Roberts*, 1995], the typical timescale of the diffusive process acting on the large scale (dimension about 1000 km) magnetic field, $\tau_D \sim 30000$ years, is found to be much larger than the secular variation timescale, $\tau_{SV} \sim 100$ years (see the recent review by *Jackson and Finlay* [2007]). The radial component of equation (1) then leads to a simple equation relating the radial magnetic field B_r at the core-mantle boundary (CMB) and the flow **u** at the top of the core (which is purely horizontal):

$$\frac{\partial B_r}{\partial t} = -\nabla_{\mathbf{H}} \cdot (\mathbf{u} B_r), \tag{2}$$

where $\nabla_{\mathbf{H}} = \nabla - \mathbf{n}\partial_r$, **n** being the unit radial outward vector. This equation has been widely used to calculate core flows from geomagnetic observations [*Bloxham and Jackson*, 1991; *Whaler*, 2007].

[4] The validity of the FF assumption has however been the subject of much debate over the years. From a theoretical point of view, it has been shown that the FF assumption fails for slowly varying core flows and/or small-scale magnetic

[1]Equipe de Géomagnétisme, Institut de Physique du Globe de Paris, CNRS, INSU, Université Paris Diderot, Paris, France.
[2]DTU Space and Niels Bohr Institute, Copenhagen, Denmark.

0148-0227/10/2009JB006994

fields [*Maus*, 2008]. The first situation is expected to arise in the case of nearly steady core flows [*Gubbins and Kelly*, 1996; *Love*, 1999]. The second situation is expected to arise if some toroidal magnetic field is being expelled from the core into the weakly conducting mantle [*Allan and Bullard*, 1966; *Gubbins*, 1996, 2007], as was observed in simple 2-D models [*Bloxham*, 1986; *Drew*, 1993] and in 3-D numerical simulations of the geodynamo [e.g., *Takahashi et al.*, 2005; *Aubert et al.*, 2008]. Such a phenomenon would be analogous to what happens to the solar magnetic field within sunspots, hence the term "core spots" coined by *Roberts and Glatzmaier* [2000]. Cyclonic columnar vortices are another process observed in various numerical simulations which would lead to large amounts of magnetic diffusion at the core surface [*Rau et al.*, 2000; *Amit et al.*, 2007; *Amit and Christensen*, 2008].

[5] On the observational side, the question is whether at least part of the magnetic diffusion predicted by theory and numerical simulations can be detected. Since the radial gradient of the magnetic field below the CMB is unknown, a direct calculation of the amount of magnetic diffusion at the core surface is not possible. What can be calculated is the integrated magnetic diffusion over patches S delimited by contours of zero radial magnetic field at the core surface (referred to as "null-flux curves") [*Backus*, 1968; *Hulot and Chulliat*, 2003]:

$$\int_S D dS = \frac{d}{dt}\int_S B_r dS, \tag{3}$$

where D is the radial component of the magnetic diffusion term in equation (1), which may be written as [e.g., *Amit and Christensen*, 2008]

$$D = \eta\left[\frac{1}{c^2}\frac{\partial^2}{\partial r^2}(r^2 B_r) + \nabla_H^2 B_r\right], \tag{4}$$

where c is the core radius and

$$\nabla_H^2 = \nabla^2 - \frac{1}{r^2}\frac{\partial}{\partial r}\left(r^2\frac{\partial}{\partial r}\right).$$

On the basis of equation (3) and geomagnetic field models downward continued to the CMB, there were claims that magnetic flux was expelled from the core beneath southern Africa between 1905.5 and 1969.5 [*Bloxham and Gubbins*, 1985] and between 1980 and 2000 [*Wardinski and Holme*, 2006]. However, error bars of radial magnetic fluxes are difficult to assess, especially when data from different origins (ground observatories, satellites) and different epochs are used.

[6] Another approach consists in calculating core field models constrained by FF, obtained by setting $D = 0$ into equation (3) for each patch delimited by a null-flux curve, and comparing the roughness and fit to the data of constrained and unconstrained models calculated from the same data sets. Since the pioneering work of *Bloxham and Gubbins* [1986], several studies have taken this approach to test the FF assumption [*Bloxham et al.*, 1989; *Constable et al.*, 1993; *O'Brien et al.*, 1997; *Jackson et al.*, 2007]. The most recent one by *Jackson et al.* [2007] used a core field model for epoch 2000 based on Ørsted satellite data as the reference model and calculated models for epochs 1980 (based on Magsat satellite data), 1945, 1915 and 1882 (based on observatory and survey measurements) with the same fluxes as the model for epoch 2000. The obtained models were found to be as simple and smooth as unconstrained models for the same epochs, without any significant increase of the misfit to the data, thus leading the authors to conclude that there is no observational ground for rejecting the FF assumption. Similar conclusions were reached by the earlier studies cited above.

[7] In the present paper we reexamine the problem of the FF assumption validity, focusing on the time interval 1980–2005. At each of the two epochs 1980 and 2005, high-precision magnetic satellite data are provided by the Magsat (1980) or Ørsted and CHAMP (2005) satellites. All three satellites provide a dense and spatially homogeneous data coverage at the selected epochs, thus making it possible to recover the core field with the highest spatial resolution (up to spherical harmonic degree 13; higher degrees are masked by the crustal field), and to detect small-scale features of the secular variation [*Hulot et al.*, 2002]. Unlike *Jackson et al.* [2007], who used a spherical triangle tesselation for representing the core field, we rely on spherical harmonics and implement the FF constraint using a penalty term, following *Bloxham and Gubbins* [1986]. We explore the model space by letting the regularization and FF constraint parameters vary, so that several FF-constrained models are obtained. While constrained models have nearly similar global RMS misfits as unconstrained models, their data residuals are higher above the South Atlantic Ocean, which we interpret as evidence of magnetic flux expulsion.

2. Data Selection and Preprocessing

[8] In our analysis we used magnetic data from the Magsat satellite between November 1979 and April 1980 and magnetic data from the Ørsted and CHAMP satellites between November 2004 and April 2005. The 1980 data set comprises of 8650 vector triplets and 9737 scalar data points (1978 of which are taken at dipole latitudes poleward of 60°). The 2005 data is a subset of the CHAOS data set [*Olsen et al.*, 2006] and comprises of 6528 vector triplets and 7809 scalar data points (1942 from dipole latitudes poleward of 60°).

[9] Both data sets have been selected using the same criteria as for the CHAOS model: (1) at all latitudes we require that the D_{st} index does not change by more than 2 nT/h; (2) at nonpolar latitudes (equatorward of ±60° dipole latitude) $Kp \leq 2o$ (where Kp is the planetary index) has to be fulfilled; (3) vector data have been taken for dipole latitudes equatorward of ±60°; and (4) scalar data were used for regions poleward of ±60° or if vector data were not available. Data sampling interval was 60 s. Finally, an equal area data selection was performed, in order to avoid using the usual $\sin\theta$ weighing in the modeling.

[10] Despite of the similarities, there are, however, also differences in data selection for the two data sets, which was necessary due to the different orbital parameters of the satellites: Both morning and evening Magsat data were used in the 1980 data set (which is the reason for the slightly larger amount of data for epoch 1980), but low-latitude (equatorward of ±40° geographic latitude) evening data were excluded, to avoid contamination by contributions from the equatorial electrojet. For the 2005 data set we used only data from dark

regions (sun 10° below horizon), and the nonpolar CHAMP data were restricted to local time past midnight. Finally, we used only Ørsted and CHAMP data in regions poleward of 60° dipole latitude if the merging electric field at the magnetopause is less than 0.8 mV/m (this condition could not be applied to the Magsat data because no information on the merging electric field is available for 1980.)

[11] Each of the two data sets span about 6 months, and in order to account for secular variation we propagated the observations of each data set to common epoch t_0. We used the secular variation of model CM4 [*Sabaka et al.*, 2004] to propagate the 1980 data to epoch t_0 = 1980.0, and the CHAOS secular variation to propagate the 2005 data to epoch t_0 = 2005.0.

[12] We also removed from each of the two data sets the lithospheric field for spherical harmonic degrees n = 15–90 (coefficients with n = 15–40 from the CHAOS model and above n = 40 from the model MF5 of *Maus et al.* [2007]) and the periodic magnetospheric field, as given by CM4. For each data set, a preliminary, unconstrained model was calculated using iteratively reweighted least squares with Huber weights [e.g., *Olsen*, 2002]. Data with Huber weights smaller than 0.8 were then removed from the data set.

3. Model Determination

[13] The magnetic field $\mathbf{B} = -\nabla V$ is derived from a magnetic scalar potential V which is expanded into terms of spherical harmonics:

$$\begin{aligned} V = {} & a\sum_{n=1}^{N_{\mathrm{MF}}}\sum_{m=0}^{n}\left(g_n^m\cos m\phi + h_n^m\sin m\phi\right)\left(\frac{a}{r}\right)^{n+1}P_n^m(\cos\theta) \\ & + a\sum_{n=1}^{2}\sum_{m=0}^{n}\left(q_n^m\cos m\phi + s_n^m\sin m\phi\right)\left(\frac{r}{a}\right)^{n}P_n^m(\cos\theta) \\ & + a\sum_{m=0}^{1}\left(\hat{q}_1^m\cos\phi + \hat{s}_1^m\sin\phi\right)\left\{E_{\mathrm{st}}(t)\left(\frac{r}{a}\right) + I_{\mathrm{st}}(t)\left(\frac{a}{r}\right)^2\right\} \\ & \cdot P_1^m(\cos\theta). \end{aligned}$$

a = 6371.2 km is the mean radius of the Earth, (r, θ, ϕ) are geocentric spherical coordinates, $P_n^m(\cos\theta)$ are the associated Schmidt seminormalized Legendre functions of degree n and order m, and (g_n^m, h_n^m) and (q_n^m, s_n^m) are the Gauss coefficients describing sources internal and external to the Earth, respectively. The last part of the above equation (coefficients $\hat{q}_1^0$, $\hat{q}_1^1$ and $\hat{s}_1^1$) accounts for the variability of contributions from the magnetospheric ring current; E_{st}, I_{st} are time series of the decomposition of the D_{st} index, $D_{\mathrm{st}}(t) = E_{\mathrm{st}}(t) + I_{\mathrm{st}}(t)$, into external and induced parts, respectively [*Maus and Weidelt*, 2004; *Olsen et al.*, 2005].

[14] The maximum degree of the model is chosen as N_{MF} = 20, resulting in 440 internal field coefficients g_n^m, h_n^m and 11 external field coefficients q_n^m, s_n^m, $\hat{q}_n^m$, $\hat{s}_n^m$, resulting in a total of 451 parameters, which are collected in the model vector $\mathbf{m}$.

[15] The regularized unconstrained models at epoch 1980 and 2005 are calculated by iterative least squares inversion, minimizing the objective function

$$\Phi(\mathbf{m}) = [\gamma - \mathbf{f}(\mathbf{m})]^T\mathbf{C}_e^{-1}[\gamma - \mathbf{f}(\mathbf{m})] + \lambda\,\mathbf{m}^T\mathbf{C}_m^{-1}\mathbf{m}, \quad (5)$$

where $\mathbf{m}$ is the model vector, γ is the data vector, $\mathbf{f}(\mathbf{m})$ is the synthetic data vector, $\mathbf{C}_e^{-1}$ is the data covariance matrix, λ is the damping parameter, and $\mathbf{C}_m^{-1}$ is the model weight matrix. The elements of the data variance matrix $\mathbf{C}_e^{-1}$ are chosen as for the CHAOS model. The model weights in $\mathbf{C}_m^{-1}$ for the Gauss coefficients of degree n describing the internal field are

$$\frac{(n+1)^2}{2n+1}\left(\frac{a}{c}\right)^{2n+4}, \quad (6)$$

where c = 3485 km is the core radius, thus imposing a minimum energy norm at the core [*Shure et al.*, 1982]; the external field coefficients are not regularized.

[16] For a given reference model $\mathbf{m}_0$, the FF constraint is applied by adding a penalty term [*Bloxham and Gubbins*, 1986],

$$\mu|\mathbf{F}(\mathbf{m}) - \mathbf{F}(\mathbf{m}_0)|^2, \quad (7)$$

to the objective function, $\Phi(\mathbf{m})$, where $\mathbf{F}(\mathbf{m})$ is the vector of radial magnetic fluxes through the patches delimited by the null-flux curves of model $\mathbf{m}$ at the core-mantle boundary, and μ is a scaling parameter. The $\mathbf{F}$ function may be expressed as the product of a matrix $\mathbf{L}^T(\mathbf{m})$ with the model vector $\mathbf{m}$:

$$\mathbf{F}(\mathbf{m}) = \mathbf{L}^T(\mathbf{m})\mathbf{m}. \quad (8)$$

This is a nonlinear function in $\mathbf{m}$. However, as the radial magnetic field vanishes on the null-flux curves, we have

$$\frac{d\mathbf{L}^T}{d\mathbf{m}}\mathbf{m} = \mathbf{0}, \quad (9)$$

hence

$$\frac{d\mathbf{F}}{d\mathbf{m}} = \mathbf{L}^T(\mathbf{m}) \quad (10)$$

on the null-flux curves, which can be used to calculate the derivative of the objective function Φ with respect to the model vector $\mathbf{m}$ and iterate the model at each step of the inversion.

[17] In order to evaluate the $\mathbf{L}$ matrix, the surface integrals giving the radial magnetic fluxes are transformed into curvilinear integrals [*Shure et al.*, 1982]:

$$\int_{S_j} B_r\,dS = \int_{\partial S_j}\mathbf{n}\cdot\nabla_h f\;dl, \quad (11)$$

where S_j is the patch delimited by the null-flux curve ∂S_j, f is chosen such that $\nabla_h^2 f = B_r$ and $\mathbf{n} = \pm\nabla_h B_r/|\nabla_h B_r|$ is a unit vector normal to ∂S_j and pointing out of the patch. The f function may be expressed as [*Jackson*, 1989]

$$f = -a\sum_{n=1}^{\infty}\frac{c}{n}\left(\frac{a}{c}\right)^{n+1}\sum_{m=0}^{n}\left[g_n^m\cos m\phi + h_n^m\sin m\phi\right)\Big]P_n^m(\cos\theta). \quad (12)$$

Substituting (12) into (11) yields the jth line of the matrix $\mathbf{L}^T(\mathbf{m})$.

[18] The penalty method does not force the model to satisfy the FF constraint exactly. In particular, null-flux curves are

Table 1. Model Statistics[a]

Epoch	λ	μ	Misfit	Norm	ΔFlux	Code
2005	0	0	2.64	40.81	N/A	N/A
	10^{-7}	0	2.65	10.62	114.0	OCd7
		10^{-19}	2.65	10.65	13.4	OCd7c19
	10^{-6}	0	2.75	10.09	103.5	OCd6
		10^{-19}	2.76	10.10	27.7	OCd6c19
		10^{-17}	2.76	10.11	10.1	OCd6c17
	10^{-5}	0	3.75	9.35	87.8	OCd5
		10^{-18}	3.78	9.36	18.1	OCd5c18
		10^{-16}	3.79	9.36	4.2	OCd5c16
1980	0	0	2.46	51.02	N/A	N/A
	10^{-7}	0	2.48	10.49	113.8	MGSd7
		10^{-19}	2.48	10.52	7.9	MGSd7c19
	10^{-6}	0	2.54	9.96	103.4	MGSd6
		10^{-19}	2.54	9.98	20.6	MGSd6c19
		10^{-17}	2.54	9.99	4.8	MGSd6c17
	10^{-5}	0	3.27	9.38	87.8	MGSd5
		10^{-18}	3.26	9.39	16.2	MGSd5c18
		10^{-16}	3.26	9.39	2.9	MGSd5c16

[a]RMS of scalar residuals (in nT) at nonpolar latitudes (less than 60°); norm $\mathbf{m}^T\mathbf{C}_m^{-1}\mathbf{m}$ (in $\times 10^{10}$ nT^2); flux difference $|\mathbf{F}(\mathbf{m}) - \mathbf{F}(\mathbf{m}_0)|$ (in MWb) with respect to the unconstrained, regularized model $\mathbf{m}_0$ at the other epoch obtained with the same value of λ.

allowed to appear, disappear, merge and break into several pieces as long as the associated change of radial magnetic flux is small. A local failure of the frozen flux associated with such an event will add to the total radial diffusion that is constrained by the penalty term. When the constraint parameter μ is large, the total radial diffusion permitted is small and the diffusion associated with the observed changes of topology of the null-flux curves is even smaller.

[19] As the topology of the null-flux curves is not fixed, it may change after the ith iteration of the inversion. It is then necessary to modify the reference flux vector $\mathbf{F}(\mathbf{m}_0)$ in order to make it the same size as the flux vector $\mathbf{F}(\mathbf{m}_i)$:

[20] 1. When a new null-flux curve appears, a zero reference flux is inserted in $\mathbf{F}(\mathbf{m}_0)$.

[21] 2. When a null-flux curve disappears, the corresponding reference flux is suppressed in $\mathbf{F}(\mathbf{m}_0)$.

[22] 3. When two null-flux curves are merged, the corresponding reference fluxes in $\mathbf{F}(\mathbf{m}_0)$ are added.

[23] 4. When a null-flux curve breaks into two pieces, one of them (the smallest) is treated as a new null-flux curve.

4. Results

[24] For each epoch (1980 and 2005), we calculated nine different models from exactly the same data set: (1) one unregularized, unconstrained model ($\lambda = \mu = 0$), (2) three regularized ($\lambda \neq 0$), but unconstrained ($\mu = 0$) models, and (3) five regularized ($\lambda \neq 0$) and FF-constrained ($\mu \neq 0$) models. The reference model for a given epoch and a given value of λ is the regularized, unconstrained model at the other epoch having the same λ. The values for μ are chosen between 10^{-16} and 10^{-19}, depending on λ. Table 1 lists the values of λ and μ for these nine models.

[25] In what follows, we analyze and compare the various properties of these 18 models: global statistics (misfit, norm, flux differences), maps of the CMB radial magnetic field, fluxes through reversed flux patches, data residuals and power spectra.

4.1. Global Statistics

[26] The nonpolar RMS misfits and norms of obtained models are given in Table 1. Also listed are the radial magnetic flux differences between each model and the corresponding reference model. A code is given to each model for later reference. As expected, increasing λ (for unconstrained models) leads to smaller norms, but also to larger misfits and smaller flux differences. The norms of unregularized models appear to be much larger than those of weakly regularized models, while their misfits are almost the same (less than 0.02 nT of difference). This suggests that unregularized models contain a lot of spurious features and for this reason they will not be considered any further. On the other hand, models with the strongest regularization ($\lambda = 10^{-5}$) have RMS misfits significantly larger than other regularized models ($\lambda = 10^{-6}$ and 10^{-7}), suggesting that they are indeed too much regularized.

[27] When the FF constraint is applied, the flux difference decreases while the norm remains the same or increases slightly (less than a few percent). The RMS misfit varies by less than 0.01 nT for $\lambda = 10^{-7}$ and 10^{-6}, and up to a few 0.01 nT for $\lambda = 10^{-5}$. The very slight decrease (0.01 nT) of misfit at epoch 1980 is counterintuitive (additional constraints are expected to lead to larger data residuals) and thus provides an estimate of the error associated with the iterative process used to solve the inverse problem. As a result, applying the FF constraint does not lead to significantly larger misfits at the global scale, which is in good agreement with results previously obtained by *Jackson et al.* [2007].

4.2. CMB Radial Magnetic Field and Magnetic Fluxes

[28] For $\lambda = 10^{-5}$, there are nine null-flux curves at the core surface in 1980 and 2005 (see Table 2 and Figures 1a and 1b). One of them is the magnetic equator while the other eight delimit reversed flux patches. Interestingly, the magnetic equator undergoes only a very small flux difference between 1980 and 2005. This may come as a surprise, as magnetic diffusion is expected to act on normal patches as much as it does on reversed flux patches (see images of *Amit and Christensen* [2008]). However, the very large size of the patch encircled by the magnetic equator makes it unsuitable to detect localized failures of the FF assumption. For example, in a given hemisphere, magnetic diffusion may act in opposite ways in two normal flux patches, thus leading to an unchanged flux through that hemisphere.

[29] By far the largest and most intense reversed flux patch is the South Atlantic/South Pole patch, which contains about 85% of the total reversed flux (in absolute value). The second largest flux is observed in the St. Helena patch, centered near 20°S, 15°W. When considering unconstrained models, these two patches undergo the largest flux differences between 1980 and 2005 of +46 and +48 MWb, respectively. The effect of the FF constraint at the CMB can be visualized by mapping the differences between the radial magnetic field of the FF-constrained model and that of the corresponding unconstrained model (Figures 1c and 1d). We find that the largest differences are concentrated within and around the St. Helena patch and, to a lesser extent, the North Pacific and Mariana patches, centered near 45°N, 170°W and 20°N, 165°E, respectively. (Note the expected sign difference between maps in Figures 1c and 1d.) What happens in the

Table 2. Absolute Fluxes Through Patches Delimited by $B_r = 0$ Curves at the CMB of Unconstrained ($\mu = 0$), Regularized Models at Epochs 1980 and 2005 and Differences Between Fluxes at 2005 and 1980[a]

	$\lambda = 10^{-5}$			$\lambda = 10^{-6}$			$\lambda = 10^{-7}$		
Patch	1980	2005	2005–1980	1980	2005	2005–1980	1980	2005	2005–1980
N/S Hemisphere	17477	17430	−47	17676	17643	−33	17818	17771	−47
South Atlantic	1335	1381	46	1416	1562	73	1497	1582	85
South Pole				73			140	136	−4
St. Helena	96	144	48	94	148	54	101	138	37
North Pole	50	65	15	79	88	9	140	109	39
Barents Sea	9	2	−7	32	42	10		70	
Mariana	38	24	−14	80	54	−26	97	76	−21
Easter	28	23	−5	25	25	0	29	27	−2
North Pacific	11	37	26	33	50	17	59	61	2
Bermuda	8	3	−5	31	15	−16	36	35	−1
Hawaii	N/A	N/A	N/A	1	0	−1	9	6	−3
Black Sea	N/A	N/A	N/A	N/A	5	5	2	17	15
Central America	N/A	N/A	N/A	N/A	N/A	N/A	6	7	1
South Pacific	N/A	N/A	N/A	N/A	N/A	N/A	4	3	−1
North Atlantic	N/A	N/A	N/A	N/A	N/A	N/A	2	N/A	−2
Ural	N/A	N/A	N/A	N/A	N/A	N/A	1	N/A	−1

[a]Absolute fluxes are given in MWb; reversed flux patches are named according to close-by geographical features (islands, oceans, etc.); see Figures 1–3. N/A indicates that the flux cannot be calculated because the corresponding patch does not exist. When no flux value is indicated, it means the patch is merged with the patch of the previous line and the flux value indicated on that line therefore applies to both lines.

South Atlantic/South Pole patch is quite different as the FF constraint leads to small-scale, weakly intense structures; the constraint has been spread out within this very large patch. There are more small-scale features in 1980 than in 2005, particularly around the St. Helena spot, indicating that the effect of the regularization is more pronounced in 2005, probably due to a smaller number of data than in 1980.

[30] Decreasing the regularization parameter λ indeed leads to smaller-scale structures, both in the CMB radial magnetic field and in the differences between CMB radial magnetic fields of constrained and unconstrained models (Figures 2 and 3). It also results in more null-flux curves and a larger overall norm, hence larger magnetic fluxes (see Table 2). For $\lambda = 10^{-6}$ and $\lambda = 10^{-7}$, the topology of the null-

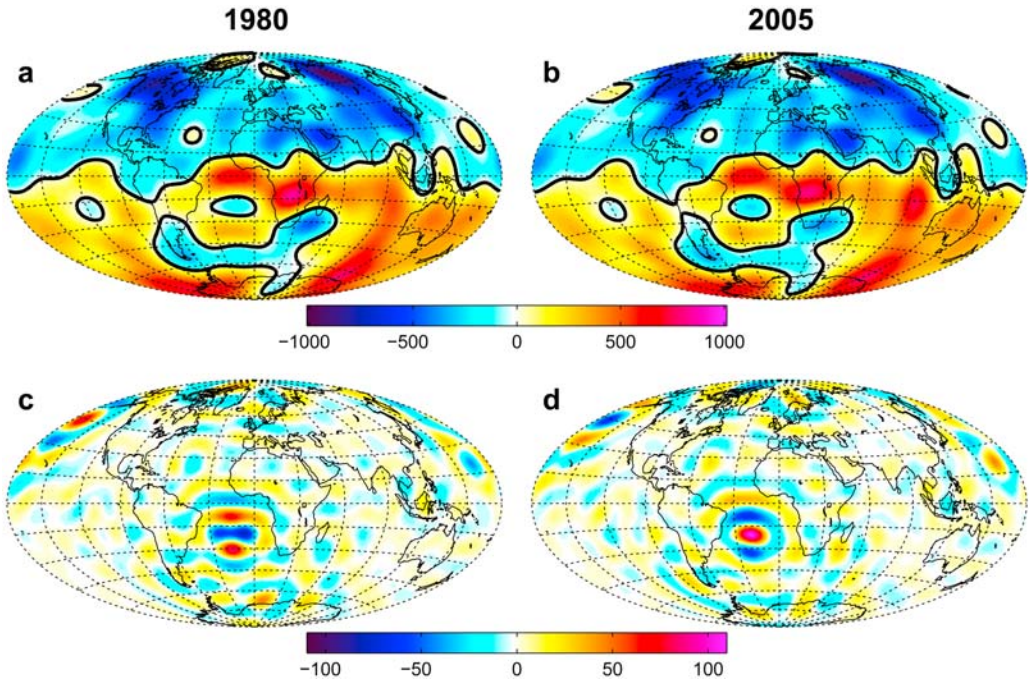

Figure 1. (a) Map of the radial magnetic field at the CMB from the unconstrained, regularized model MGSd5 ($\lambda = 10^{-5}$, epoch 1980). Null-flux curves are represented by black lines. (b) Same for model OCd5 ($\lambda = 10^{-5}$, epoch 2005). (c) Map of the difference between the radial magnetic field at the CMB from model MGSd5c16 ($\lambda = 10^{-5}$, $\mu = 10^{-16}$, epoch 1980) and that from model MGSd5. (d) Same as Figure 1c except for models OCd5c16 ($\lambda = 10^{-5}$, $\mu = 10^{-16}$, epoch 2005) and model OCd5. Magnetic fields are expressed in μT.

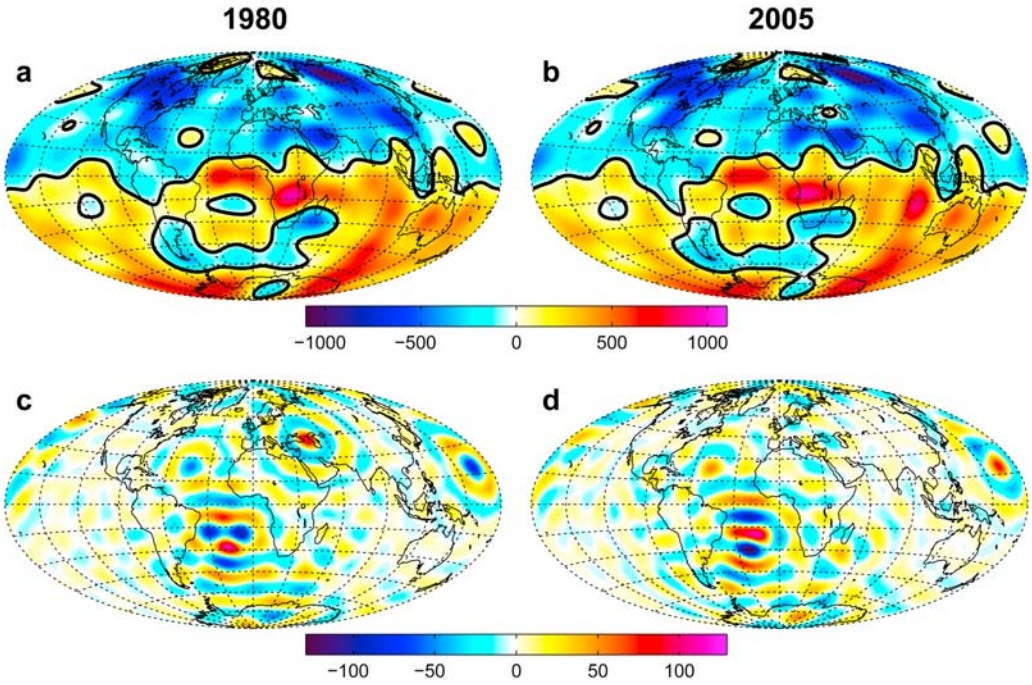

Figure 2. Same as Figure 1 except with $\lambda = 10^{-6}$, $\mu = 10^{-17}$.

flux curves actually changes over the 25 years between 1980 and 2005. For $\lambda = 10^{-6}$, the South Atlantic and South Pole patches merge, while a new patch appears beneath the Black Sea, leaving the total number of curves unchanged at 11. For $\lambda = 10^{-7}$, the combined North Pole/Barents Sea patch splits into two patches, while the North Atlantic and Ural patches disappear (patches having fluxes less than 1 MWb are not considered). However, none of these changes leads to flux differences as large as those observed within the South Atlantic/South Pole patch (be it merged or split) and the St. Helena patch, except the combined North Pole/Barents Sea patch for $\lambda = 10^{-7}$. This can also be seen from the flux difference maps in Figures 2c, 2d, 3c,and 3d, where the most intense structures are located in the South Atlantic area and, for $\lambda = 10^{-7}$, near the Barents Sea patch. The absolute flux increases between 1980 and 2005 in the South Atlantic/South

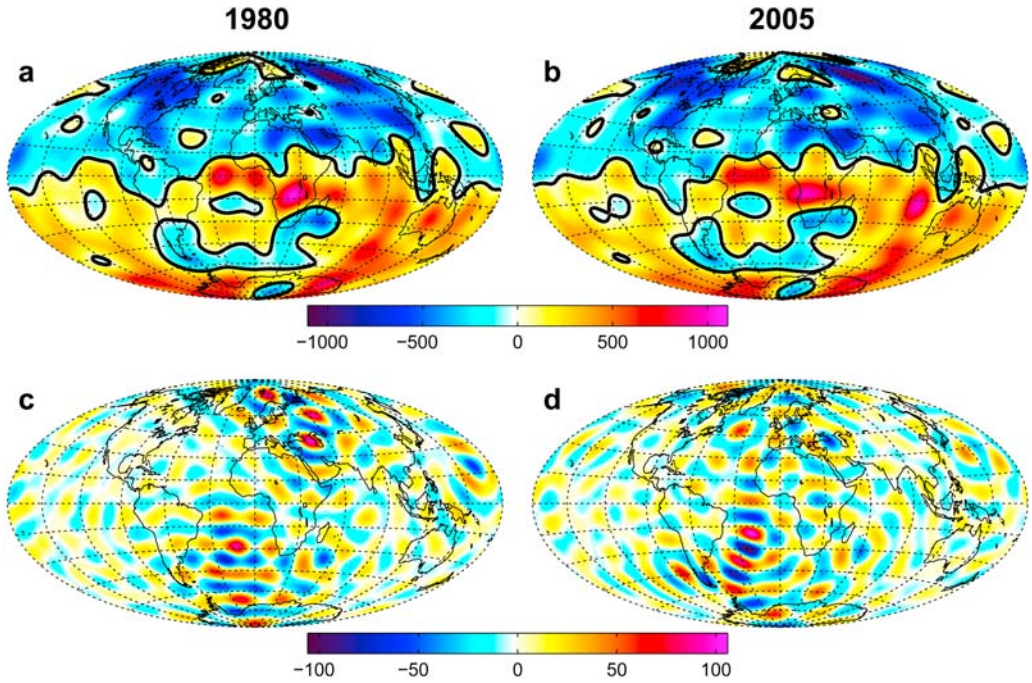

Figure 3. Same as Figure 1 except with $\lambda = 10^{-7}$, $\mu = 10^{-19}$.

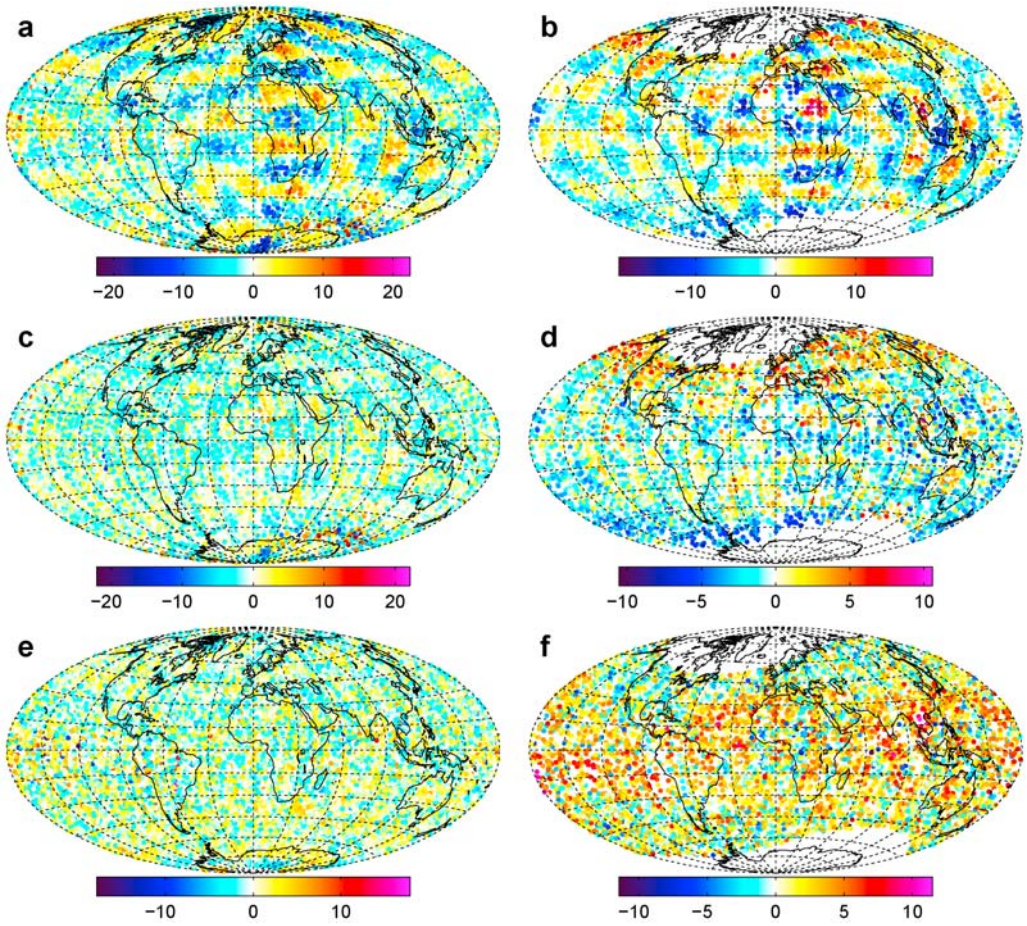

Figure 4. Maps of data residuals (expressed in nT) for (a) the field intensity and (b) the radial field from model OCd5 ($\lambda = 10^{-5}$, epoch 2005). (c, d) Same as Figures 1a and 1b except from model OCd6 ($\lambda = 10^{-6}$, epoch 2005). (e, f) Same as Figures 1a and 1b except from model MGSd6 ($\lambda = 10^{-6}$, epoch 1980).

Pole and St. Helena patches are the most robust flux changes over this time interval. The ones occurring in the North Pole/Barents Sea, Mariana, and, to a lesser extent, Black Sea are more model-dependent.

4.3. Data Residuals

[31] In order to better characterize the robustness of the observed flux differences, we systematically mapped the data residuals of each model at satellite altitude. We considered two types of residuals: those for the field intensity (dF, from vector and scalar data) and those for the radial field (dB_r, only vector data). Each type has its advantage: the field intensity is expected to be unaffected by ionospheric field-aligned currents; extrema in B_r at satellite altitude are located exactly vertical to extrema in B_r at the CMB, due to the Green's function for that component [*Constable et al.*, 1993].

[32] We first look at the data residuals of unconstrained models. As expected, residuals for $\lambda = 10^{-5}$ are larger than those for $\lambda = 10^{-6}$, as is shown in Figures 4a–4d for epoch 2005. Residuals for $\lambda = 10^{-5}$ reach their largest absolute values (about 20 nT) within small-scale structures corresponding to degrees $n = 10$ to 15 (approximately) and distributed all over the Earth's surface. On the other hand, the $\lambda = 10^{-6}$ model has much smaller dF residuals, not exceeding about 5 nT in absolute value over most of the Earth's surface. The dB_r residuals are larger, especially in the subauroral regions, probably due to the effect of external currents. When further decreasing λ to 10^{-7}, no significant improvement can be seen in the data residuals (not shown). Thus the $\lambda = 10^{-6}$ model seems to be the best unconstrained model for 2005, i.e., the simplest model describing the data with the minimum misfit.

[33] The $\lambda = 10^{-6}$ regularization parameter is also the best compromise for epoch 1980. Corresponding data residuals are mapped in Figures 4e and 4f. Unlike in 2005, the largest dB_r residuals are concentrated at midlatitudes to low latitudes in 1980. These residuals could be caused by external currents flowing in the evening in the equatorial region, as the Magsat satellite was in a dusk-dawn orbit, or by a lower attitude precision of Magsat data.

[34] We now look at the differences between data residuals for unconstrained and FF-constrained models. We consider (1) differences between absolute scalar residuals and (2) differences between radial magnetic field residuals. Results for 2005 and 1980 are displayed in Figures 5 and 6, respectively. Differences of type 1 are positive (negative) if the FF-constrained model is closer (further) to the data than the unconstrained model. Differences of type 2 represent the local

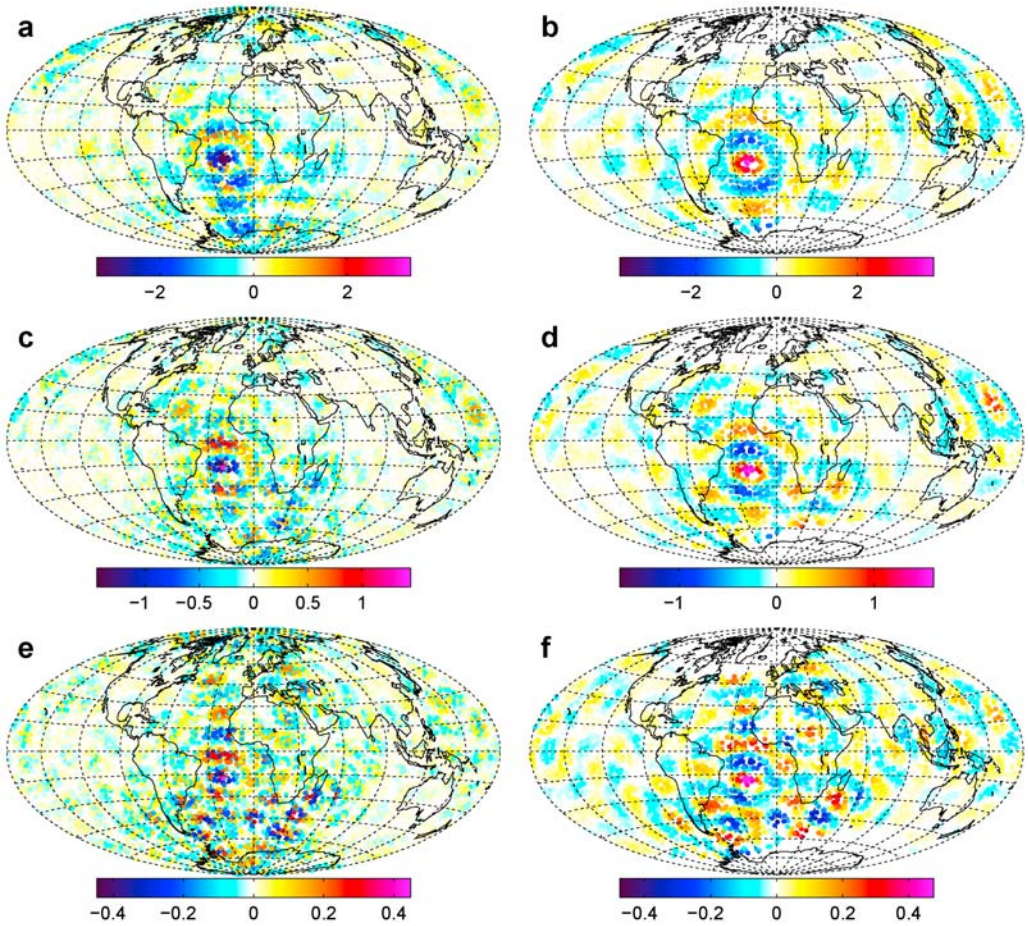

Figure 5. Maps of differences between (a) absolute scalar residuals (in nT) and (b) radial magnetic field residuals (in nT), from models OCd5 ($\lambda = 10^{-5}$, $\mu = 0$, epoch 2005) and OCd5c16 ($\lambda = 10^{-5}$, $\mu = 10^{-16}$, epoch 2005). (c, d) Same as Figures 2a and 2b except for models OCd6 ($\lambda = 10^{-6}$, $\mu = 0$, epoch 2005) and OCd6c17 ($\lambda = 10^{-6}$, $\mu = 10^{-17}$, epoch 2005). (e, f) Same as Figures 2a and 2b except for models OCd7 ($\lambda = 10^{-7}$, $\mu = 0$, epoch 2005) and OCd7c19 ($\lambda = 10^{-7}$, $\mu = 10^{-19}$, epoch 2005).

effect of the FF constraint at satellite altitude, as they are in fact equal to differences between model predictions from the constrained and unconstrained models at each data point:

$$\begin{aligned}(dB_r)_{OCd5} - (dB_r)_{OCd5c16} &= \left[(B_r)_{OCd5} - (B_r)_{data}\right] \\ &\quad - \left[(B_r)_{OCd5c16} - (B_r)_{data}\right] \\ &= (B_r)_{OCd5} - (B_r)_{OCd5c16}.\end{aligned}$$

[35] For $\lambda = 10^{-5}$, epoch 2005, the effect of the FF constraint at satellite altitude peaks above the St. Helena patch, where it reaches about 4 nT (Figure 5b). The structure of the corresponding radial field difference at the CMB (Figure 1d) is easily recognizable. There is no other region where the effect of the constraint is larger than 2 nT. The differences between absolute scalar residuals are mostly negative above the St. Helena and South Atlantic/South Pole patches, reaching about −3 nT (Figure 5a). In order to better quantify this effect, we calculated the RMS of scalar residuals and the mean of radial field residuals in a region above the St. Helena patch defined by $105° \le \theta \le 115°$ (colatitude) and $330° \le \phi \le 360°$ (longitude). When μ increases from 0 to 10^{-16}, the RMS of the intensity residuals increases by 1.56 nT and the mean dB_r decreases by 1.65 nT (Table 3), in good agreement with the visual inspection of the maps.

[36] For $\lambda = 10^{-6}$, the effect of the FF constraint at satellite altitude is smaller and less focused. It still peaks above the St. Helena patch, at about 1.5 nT, and there is another, smaller peak above the Mariana patch (Figure 5d). The scalar residuals are enhanced by the FF constraint, as can be seen in Figure 5c, where the spot above the St. Helena patch is mostly blue. However, this spot is surrounded by several red spots indicating a local decrease of the scalar residuals. The values of RMS dF increase by only 0.26 nT within the St. Helena region, while the mean dB_r decreases by 0.76 nT. Although less conspicuous than for $\lambda = 10^{-5}$, the effect of the FF constraint is still detectable.

[37] For $\lambda = 10^{-7}$, the effect of the constraint becomes very weak at satellite altitude (less than 0.5 nT) and is no more focused above the St. Helena patch (Figure 5f), due to the spreading of the small-scale structures at the CMB (Figure 3d). As a result, no clear deterioration of the local misfit can be detected, neither above St. Helena nor in any other region. The regional misfit values (Table 3) do confirm

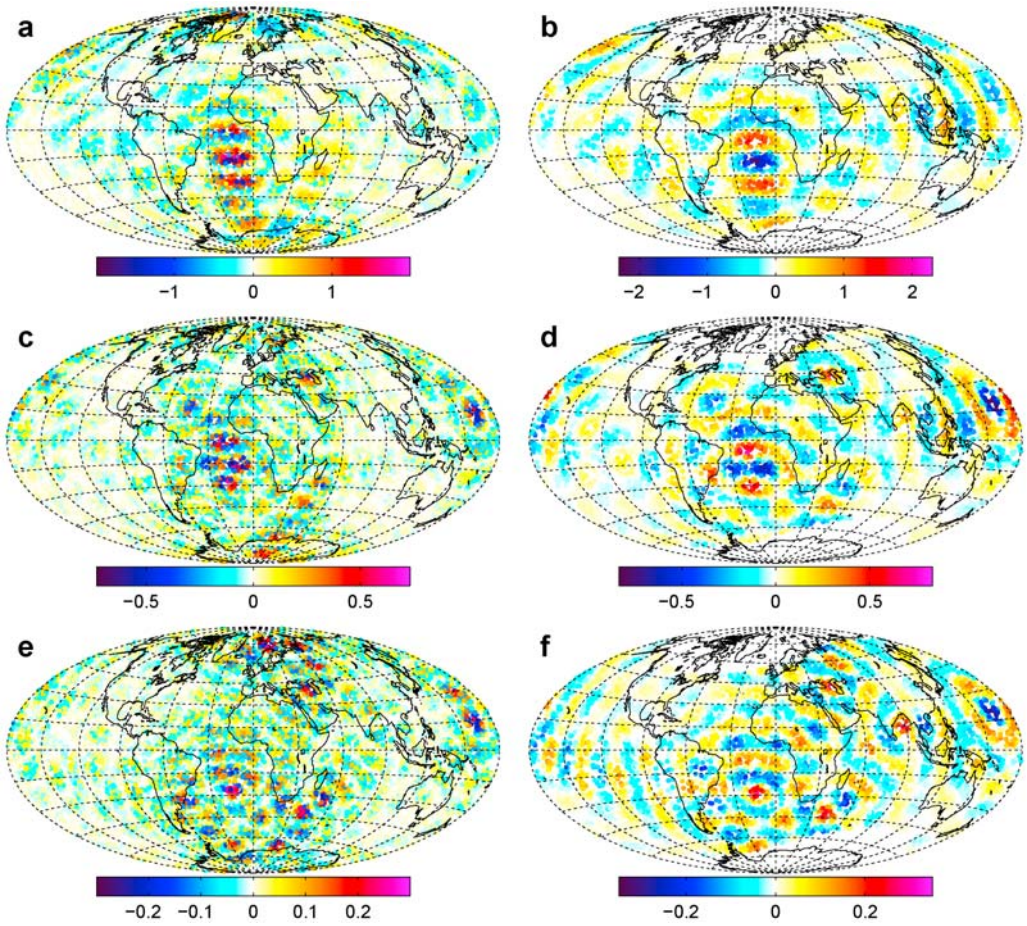

Figure 6. Same as Figure 5 except for epoch 1980.

Table 3. Model Statistics Above the St. Helena Reversed Flux Patch, in the Region Defined by $105° \le \theta \le 115°$ (Colatitude) and $330° \le \phi \le 360°$ (Longitude)[a]

Epoch	λ	μ	RMS dF	Mean dB_r	ΔFlux
2005	10^{-7}	0	1.89	0.32	36.75
		10^{-19}	1.94	0.13	6.47
	10^{-6}	0	1.84	0.16	53.99
		10^{-19}	1.97	−0.31	22.25
		10^{-17}	2.10	−0.60	7.99
	10^{-5}	0	3.47	−3.40	47.56
		10^{-18}	4.61	−4.66	12.59
		10^{-16}	5.03	−5.05	1.23
1980	10^{-7}	0	2.33	1.42	36.75
		10^{-19}	2.33	1.45	1.09
	10^{-6}	0	2.30	1.22	53.99
		10^{-19}	2.35	1.52	13.66
		10^{-17}	2.37	1.62	0.08
	10^{-5}	0	2.64	−0.74	47.56
		10^{-18}	2.62	0.14	11.00
		10^{-16}	2.65	0.38	1.45

[a]Local RMS of residuals (in nT) for the field intensity (dF, from vector and scalar data); local mean of residuals (in nT) for the radial field (dB_r). Flux difference through the St. Helena patch (in MWb) with respect to the unconstrained, regularized (with the same λ) model at the other epoch.

the visual inspection, although a very small increase of 0.05 nT of the RMS misfit is still detected. Thus there seems to be a detection threshold for the FF constraint effect at satellite altitude, below which no significant improvement of the misfit is observed. For epoch 2005, the value of this threshold is around 1 nT.

[38] The results for epoch 1980 show the same weakening of the FF constraint effect at satellite altitude when λ decreases, but the effect for a given λ is between 30% and 50% smaller (Table 3 and Figures 6b, 6d, and 6f). This can be explained by the larger number of data in 1980, which for the same λ leads to a weaker effective regularization. The major difference with epoch 2005 is the detection threshold, which seems to be around 2 nT rather than 1 nT. As a result, no significant deterioration of the misfit is observed, neither on the maps (Figures 6a, 6c, and 6e) nor in the regional RMS values in the St. Helena region (Table 3). This is probably due to the less good quality of the (vector) data in 1980, particularly in the midlatitude to low-latitude region as is shown in Figure 4f.

4.4. Power Spectra

[39] The Mauersberger-Lowes power spectra [*Lowes*, 1966] at the Earth's surface of the obtained models for epoch 2005 are shown in Figure 7. Only degrees $n \ge 10$ are shown, as there is no noticeable difference among models for $n < 10$. As previously noted, the unregularized model (blue

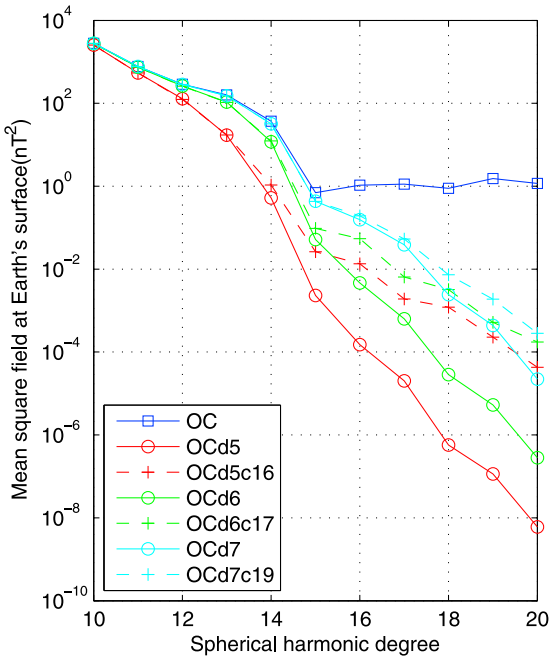

Figure 7. Power spectra at the Earth's surface of FF-constrained and -unconstrained models at epoch 2005 (degrees above $n = 10$). See Table 1 for model codes.

curve) has too much energy above $n = 15$ to be realistic. The effect of the regularization with $\lambda = 10^{-5}$ becomes noticeable for $n \geq 11$, while the $\lambda = 10^{-6}$ and $\lambda = 10^{-7}$ models separate at degree 13. The effect of the FF constraint is comparable to that of partly relaxing the regularization, but becomes noticeable at higher degrees: $n = 14$ for $\lambda = 10^{-5}$, $n = 15$ for $\lambda = 10^{-6}$, $n = 16$ for $\lambda = 10^{-7}$.

[40] We also calculated the power spectra of secular variation (SV) models obtained by taking the differences between unconstrained models at 1980 and 2005, and that of the differences between FF-constrained and -unconstrained models at epoch 2005 (Figure 8). The latter can be seen as a magnetic diffusion spherical harmonics model, since the average SV over 25 years associated with each of the FF-constrained model satisfies equation (2). It peaks at $n = 12$ for $\lambda = 10^{-5}$, $n = 14$ for $\lambda = 10^{-6}$ and $n = 16$ for $\lambda = 10^{-7}$. These degrees correspond to the scales of the dominant structures in Figures 1c, 1d, 3c, and 3d. It is clear from this graph that it becomes more difficult to detect the effect of the FF constraint when one increases λ.

5. Discussion

[41] The obtained magnetic flux variations through the St. Helena patch (Table 2) are in good agreement with recent results from *Wardinski and Holme* [2006], who found a 42 MWb increase over the 1980–2000 time interval. However, the absolute flux in 1980 is lower by at least 20% in their model, which is probably due to a different modeling method. They used a time-varying core field model based upon observatory data, constrained at both ends by two field models calculated from satellite data at epochs 1980 and 2000; the effect on magnetic fluxes at the CMB of both the temporal regularization and the a priori models is difficult to predict. Our result for epoch 1980 is more in agreement with that of *Bloxham and Gubbins* [1986], who found 88 MWb using a model based on Magsat data. The same authors found fluxes of 0 and 50 MWb in 1959.5 and 1969.5, respectively, suggesting a possible decrease of the flux expulsion rate, from about 4 MWb/yr over 1960–1980 to 2 MWb/yr over 1980–2000 (see Table 2).

[42] Our results are also in good agreement with those of *Bloxham and Gubbins* [1986] regarding the South Atlantic/

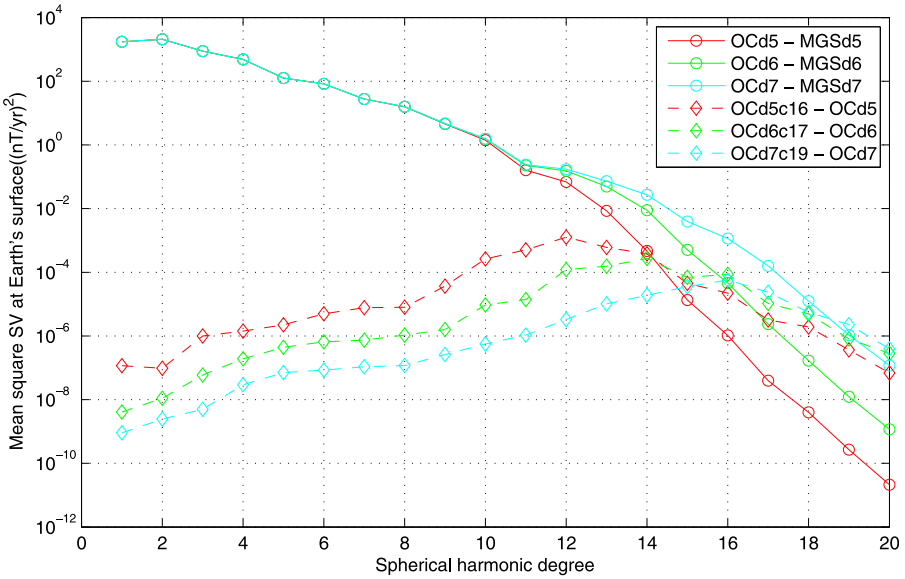

Figure 8. Power spectra at the Earth's surface of secular variation models obtained by taking the difference between models at epochs 2005 and 1980; power spectra of differences between FF-constrained and -unconstrained models at epoch 2005. See Table 1 for model codes.

South Pole patch. They find a total absolute flux of 1274 MWb in 1980, while we obtain between 1335 MWb ($\lambda = 10^{-5}$) and 1637 MWb ($\lambda = 10^{-7}$), depending on the level of regularization. Like for the St. Helena patch, there seems to be a decrease in the flux expulsion rate, from about 6 MWb/yr over 1960–1980 (their study) to about 2 to 3 MWb/yr over 1980–2000 (see Table 2). For the same combined patch, *Wardinski and Holme* [2006] found a total flux of only 649.1 MWb in 1980 and could not calculate the flux in 2000 due to the merging of the South Atlantic and Northern Hemisphere patches in 1997 in their model.

[43] In the present study, we found that the FF constraint leads to a negligible increase of the global, RMS misfit, whatever the regularization parameter. *Jackson et al.* [2007] reached a similar conclusion when applying the FF constraint to the time interval 1980–2000 and using satellite (Magsat and Ørsted) data. However, they used a very different modeling methodology (spherical triangle tesselation instead of spherical harmonics, forced preservation of the topology of the $B_r = 0$ curves instead of free merging and splitting, simultaneous constraining of the radial vorticity, exact imposition of the FF constraints up to a zero flux difference), which indicates that this is indeed a very robust result. Interestingly, and despite the different methodology, they obtained magnetic fluxes through the St. Helena and South Atlantic/South Pole patches at epoch 2000 close to our results for $\lambda = 10^{-5}$ (see Table 2): 143.5 and 1317.5 MWb, respectively. Our study therefore confirms that the FF constraint is a weak constraint at the global scale. Increasing the length of the time span is expected to lead to larger flux differences, hence stronger constraints, but this effect is counterbalanced by the less homogeneous and less dense coverage of observatory data with respect to satellite data, and by the less good quality of other types of data; this probably explains the absence of global misfit increase noted in earlier studies [*Bloxham et al.*, 1989; *Constable et al.*, 1993; *O'Brien et al.*, 1997; *Jackson et al.*, 2007]. Note that the conservation of the total unsigned flux through the CMB, which is a necessary but not sufficient condition for the FF assumption to apply [*Hide*, 1978], is an even weaker constraint. Therefore it is not surprising that no failure of the FF assumption could be detected using this constraint up to now [e.g., *Holme and Olsen*, 2006].

[44] The main result of this study is the detectable increase of scalar residuals over the St. Helena area when constraining the "best" model for epoch 2005 to satisfy the FF assumption. By best we mean the simplest model having the smallest data residuals (i.e., the one obtained with $\lambda = 10^{-6}$). This strongly suggests that the FF assumption indeed fails in the St. Helena area, in good agreement with the time evolution of the magnetic flux obtained by direct calculation at different epochs. The approach of investigating regional changes in the misfit in order to detect possible local failures of the FF assumption has never been used before (to our knowledge). The only study of the FF assumption where data residuals were mapped is that of *O'Brien et al.* [1997]. As can be seen in their Figure 6, the FF constraint leads to a slight increase in the magnitude of the residuals with respect to the vertical component over the St. Helena patch. However, no map of the scalar residuals is provided; it would be particularly interesting to plot such maps for the FF-constrained models obtained by previous studies of this kind.

[45] Within the St. Helena patch, the cumulated secular variation over $\Delta t = 25$ years that violates the frozen flux assumption, $\Delta B_r \approx 100\mu$T, reaches about 50% of the magnetic field value $B_r \approx 200\mu$T (Figures 2b and 2d). Assuming that it entirely comes from the radial diffusion of B_r due to a large radial gradient of B_r (see equation (4)), the corresponding spatial scale of magnetic field variations obtained from dimensional analysis is

$$l = \sqrt{\eta \Delta t \frac{B_r}{\Delta B_r}} \approx 56 \text{ km} \tag{13}$$

(with $\eta = 2$ m^2/s), which is much smaller than the observable horizontal spatial scales of the core field (>1000 km, corresponding to spherical harmonic degrees ≤13). Equation (13) provides an estimate of the thickness of the magnetic boundary layer [*Jault and Le Mouël*, 1991] in the St. Helena patch area, where it is expelled from the core. The corresponding magnetic Reynolds number is $R_m = Ul/\eta = O(10)$, where $U \sim 5 \times 10^{-4}$ m/s is the usual order of magnitude of the velocity of core flows [*Bloxham and Jackson*, 1991]. It is smaller than the critical Reynolds number for dynamo action. This suggests that the magnetic field is generated at depth, far from the magnetic boundary layer, as was observed by *Amit and Christensen* [2008] in numerical simulations.

[46] The observation of a possible flux expulsion through the St. Helena patch over 25 years supports the idea that the observed rapid dipole decrease (by about 5% per century since 1840) is caused by the growth of reverse magnetic flux patches in the Southern Hemisphere [*Gubbins*, 1987; *Gubbins et al.*, 2006], although advection may also weaken the axial dipole by moving normal flux to the equator or reversed flux to the poles [*Olson and Amit*, 2006]. There could be other, undetected magnetic flux expulsions at the core surface within larger patches than that of St. Helena, as the FF constraint is more easily fulfilled in large patches by simply redistributing energy in the higher spherical harmonic degrees of the model. It has been proposed in the past that this mechanism could be particularly important during excursions and reversals [*Gubbins*, 1987; *Hulot et al.*, 2002].

[47] The results of the present study also have practical implications for the calculation of core surface flows, which are usually based upon the FF assumption (although formalisms for taking into account magnetic diffusion exist [see *Gubbins*, 1996; *Amit and Christensen*, 2008]). If the core field models are optimally regularized (with respect to the data residuals), the FF assumption fails over the St. Helena patch, thus introducing some error in the flow model at this location. Assuming that magnetic diffusion only occurs within the St. Helena patch, this error will remain small and localized, as the cumulated secular variation over 1980–2005 attributed to diffusion within this patch, $\Delta B_r \approx 100\mu$T, is only a fraction of the maximum cumulated secular variation at the core surface, about $\Delta B_r \approx 320\mu$T in a nearby area located below South Africa [see, e.g., *Hulot et al.*, 2002, Figure 2a]. In order to avoid this error, one can use less regularized or FF-constrained core field models. Note that the frozen flux constraints obtained by setting $D = 0$ into equation (3) may also be written as

$$\int_S \frac{\partial B_r}{\partial t} dS = 0, \tag{14}$$

which could be implemented as a constraint in secular variation models in a similar way as for field models.

6. Conclusion

[48] In the present paper we have investigated the validity of the FF assumption between epochs 1980 and 2005, using data from the Magsat, Ørsted and CHAMP satellites, and relying on the set of necessary and sufficient conditions obtained by *Backus* [1968]. Our results can be summarized as follows:

[49] 1. Only two reversed flux patches (South Atlantic/South Pole and St. Helena) have a consistently increasing radial magnetic flux over 1980–2005, independent from the level of regularization of the core field models calculated at epochs 1980 and 2005.

[50] 2. Over the 1980–2005 time interval, using high-precision satellite data at both ends, the FF constraint has no significant effect on the global misfit.

[51] 3. Applying the FF constraint to the best unconstrained models for 2005 (i.e., the simplest model having the minimum data residuals) leads to a detectable increase of the scalar data residuals over the St. Helena area.

[52] 4. Applying the FF constraint to a less regularized model and/or to models at epoch 1980 leads to local modifications of the scalar residuals below the detection threshold.

[53] 5. In the spectral space, the smaller the regularization, the larger the degrees on which the FF constraint has a significant effect.

[54] 6. The rate of magnetic flux expulsion through both the St. Helena and the South Atlantic/South Pole reversed flux patches decreased from 1960–1980 to 1980–2005.

[55] The third result strongly suggests that the FF assumption indeed fails in the St. Helena area, where some toroidal magnetic field might be expelled from the core. This observation is in good agreement with theoretical predictions regarding the existence of core spots analogous to "sunspots" at the core surface, and supports the interpretation of the geomagnetic dipole decay in terms of magnetic flux expulsion from the southern hemisphere of the core.

[56] Because of the small number (about 10) of $B_r = 0$ curves at the core surface, the FF constraint is a weak constraint on the global scale. In order to circumvent this difficulty, one could use an additional assumption such as tangentially geostrophic assumption [*Le Mouël*, 1984], which leads to a much larger set of constraints [*Chulliat and Hulot*, 2001; *Chulliat*, 2004]. The present study suggests that failures of the combined frozen flux/tangentially geostrophic assumption could be detected.

[57] Another limitation comes from the short observational time span (with respect to the diffusive timescale). Combining data from the present satellite missions and from the upcoming Swarm mission [*Friis-Christensen et al.*, 2006] will help characterizing this phenomenon on longer timescales.

[58] **Acknowledgments.** The research reported here was financially supported by CNES and by the French embassy in Denmark. We thank Hagai Amit and an anonymous reviewer for constructive comments. This is IPGP contribution 2585.

References

Allan, D. W., and E. C. Bullard (1966), The secular variation of the Earth's magnetic field, *Proc. Cambridge Philos. Soc.*, *62*, 783–809, doi:10.1017/S0305004100040494.

Amit, H., and U. R. Christensen (2008), Accounting for magnetic diffusion in core flow inversions from geomagnetic secular variation, *Geophys. J. Int.*, *175*, 913–924, doi:10.1111/j.1365-246X.2008.03948.x.

Amit, H., P. Olson, and U. R. Christensen (2007), Tests of core flow imaging methods with numerical dynamos, *Geophys. J. Int.*, *168*, 27–39, doi:10.1111/j.1365-246X.2006.03175.x.

Aubert, J., J. Aurnou, and J. Wicht (2008), The magnetic structure of convection-driven numerical dynamos, *Geophys. J. Int.*, *172*, 945–956, doi:10.1111/j.1365-246X.2007.03693.x.

Backus, G. E. (1968), Kinematics of geomagnetic secular variation in a perfectly conducting core, *Philos. Trans. R. Soc. London, Ser. A*, *263*, 239–266, doi:10.1098/rsta.1968.0014.

Bloxham, J. (1986), The expulsion of magnetic flux from the Earth's outer core, *Geophys. J. R. Astron. Soc.*, *87*, 669–678.

Bloxham, J., and D. Gubbins (1985), The secular variation of Earth's magnetic field, *Nature*, *317*, 777–781, doi:10.1038/317777a0.

Bloxham, J., and D. Gubbins (1986), Geomagnetic field analysis—IV. Testing the frozen-flux hypothesis, *Geophys. J. R. Astron. Soc.*, *84*, 139–152.

Bloxham, J., and A. Jackson (1991), Fluid flow near the surface of Earth's outer core, *Rev. Geophys.*, *29*, 97–120, doi:10.1029/90RG02470.

Bloxham, J., D. Gubbins, and A. Jackson (1989), Geomagnetic secular variation, *Philos. Trans. R. Soc. London, Ser. A*, *329*, 415–502, doi:10.1098/rsta.1989.0087.

Braginsky, S. I., and P. H. Roberts (1995), Equations governing convection in Earth's core and the geodynamo, *Geophys. Astrophys. Fluid Dyn.*, *79*, 1–97, doi:10.1080/03091929508228992.

Chulliat, A. (2004), Geomagnetic secular variation generated by a tangentially geostrophic flow under the frozen-flux assumption—II. Sufficient conditions, *Geophys. J. Int.*, *157*, 537–552, doi:10.1111/j.1365-246X.2004.02216.x.

Chulliat, A., and G. Hulot (2001), Geomagnetic secular variation generated by a tangentially geostrophic flow under the frozen-flux assumption—I. Necessary conditions, *Geophys. J. Int.*, *147*, 237–246, doi:10.1046/j.1365-246X.2001.00535.x.

Constable, C. G., R. L. Parker, and P. Stark (1993), Geomagnetic field models incorporating frozen-flux constraints, *Geophys. J. Int.*, *113*, 419–433, doi:10.1111/j.1365-246X.1993.tb00897.x.

Drew, S. J. (1993), Magnetic field expulsion into a conducting mantle, *Geophys. J. Int.*, *115*, 303–312, doi:10.1111/j.1365-246X.1993.tb05604.x.

Friis-Christensen, E., H. Lühr, and G. Hulot (2006), Swarm: A constellation to study the Earth's magnetic field, *Earth Planets Space*, *58*, 351–358.

Gubbins, D. (1987), Mechanisms of geomagnetic polarity reversals, *Nature*, *326*, 167–169, doi:10.1038/326167a0.

Gubbins, D. (1996), A formalism for the inversion of geomagnetic data for core motions with diffusion, *Phys. Earth Planet. Inter.*, *98*, 193–206, doi:10.1016/S0031-9201(96)03187-1.

Gubbins, D. (2007), Geomagnetic constraints on stratification at the top of the Earth's core, *Earth Planets Space*, *59*, 661–664.

Gubbins, D., and P. Kelly (1996), A difficulty with using the frozen flux hypothesis to find steady core motions, *Geophys. Res. Lett.*, *23*, 1825–1828, doi:10.1029/96GL01392.

Gubbins, D., and P. H. Roberts (1987), Magnetohydrodynamics of the Earth's core, in *Geomagnetism*, vol. 2, edited by J. Jacobs, pp. 1–183, Academic, London.

Gubbins, D., A. L. Jones, and C. C. Finlay (2006), Fall in Earth's magnetic field is erratic, *Science*, *312*, 900–902, doi:10.1126/science.1124855.

Hide, R. (1978), How to locate the electrically conducting fluid core of a planet from external magnetic observations, *Nature*, *271*, 640–641, doi:10.1038/271640a0.

Holme, R., and N. Olsen (2006), Core surface flow modelling from high-resolution secular variation, *Geophys. J. Int.*, *166*, 518–528, doi:10.1111/j.1365-246X.2006.03033.x.

Hulot, G., and A. Chulliat (2003), On the possibility of quantifying diffusion and horizontal Lorentz forces at the Earth's core surface, *Phys. Earth Planet. Inter.*, *135*, 47–54, doi:10.1016/S0031-9201(02)00191-7.

Hulot, G., C. Eymin, B. Langlais, M. Mandea, and N. Olsen (2002), Small-scale structure of the geodynamo inferred from Ørsted and Magsat satellite data, *Nature*, *416*, 620–623, doi:10.1038/416620a.

Jackson, A. (1989), The Earth's magnetic field at the core-mantle boundary, Ph.D. thesis, Univ. of Cambridge, Cambridge, U. K.

Jackson, A., and C. C. Finlay (2007), Geomagnetic Secular Variation and Its Applications to the Core, in *Treatise of Geophysics*, vol. 5, *Geomagnetism*, edited by M. Kono, pp. 147–193, Elsevier, Amsterdam, doi:10.1016/B978-044452748-6.00090-0.

Jackson, A., C. G. Constable, M. R. Walker, and R. L. Parker (2007), Models of Earth's main magnetic field incorporating flux and radial vorticity con-

straints, *Geophys. J. Int.*, *171*, 133–144, doi:10.1111/j.1365-246X.2007.03526.x.

Jault, D. and J.-L. Le Mouël (1991), Physical properties at the top of the core and core surface motions, *Phys. Earth Planet. Inter.*, *68*, 76–84, doi:10.1016/0031-9201(91)90009-7.

Le Mouël, J.-L. (1984), Outer core geostrophic flow and secular variation of Earth's geomagnetic field, *Nature*, *311*, 734–735, doi:10.1038/311734a0.

Love, J. J. (1999), A critique of frozen-flux inverse modelling of a nearly steady geodynamo, *Geophys. J. Int.*, *138*, 353–365, doi:10.1046/j.1365-246x.1999.00895.x.

Lowes, F. (1966), Mean-square values on sphere of spherical harmonic vector fields, *J. Geophys. Res.*, *71*, 2179, doi:10.1029/JZ071i008p02179.

Maus, S. (2008), On the applicability of the frozen flux approximation in core flow modelling as a function of temporal frequency and spatial degree, *Geophys. J. Int.*, *175*, 853–856, doi:10.1111/j.1365-246X.2008.03972.x.

Maus, S., and P. Weidelt (2004), Separating the magnetospheric disturbance magnetic field into external and transient internal contributions using a 1D conductivity model of the Earth, *Geophys. Res. Lett.*, *31*, L12614, doi:10.1029/2004GL020232.

Maus, S., H. Lühr, M. Rother, K. Hemant, G. Balasis, P. Ritter and C. Stolle (2007), Fifth generation lithospheric magnetic field model from CHAMP satellite measurements, *Geochem. Geophys. Geosyst.*, *8*, Q05013, doi:10.1029/2006GC001521.

O'Brien, M. S., C. G. Constable, and R. L. Parker (1997), Frozen-flux modelling for epochs 1915 and 1980, *Geophys. J. Int.*, *128*, 434–450, doi:10.1111/j.1365-246X.1997.tb01566.x.

Olsen, N. (2002), A model of the geomagnetic field and its secular variation for epoch 2000 estimated from Ørsted data, *Geophys. J. Int.*, *149*, 454–462, doi:10.1046/j.1365-246X.2002.01657.x.

Olsen, N., T. J. Sabaka, and F. Lowes (2005), New parameterization of external and induced fields in geomagnetic field modeling, and a candidate model for IGRF 2005, *Earth Planets Space*, *57*, 1141–1149.

Olsen, N., H. Lühr, T. J. Sabaka, M. Mandea, M. Rother, L. Tøffner-Clausen and S. Choi (2006), CHAOS—A model of the Earth's magnetic field derived from CHAMP, Ørsted and SAC-C magnetic satellite data, *Geophys. J. Int.*, *166*, 67–75, doi:10.1111/j.1365-246X.2006.02959.x.

Olson, P., and H. Amit (2006), Changes in Earth's dipole, *Naturwissenschaften*, *93*, 519–542, doi:10.1007/s00114-006-0138-6.

Rau, S., U. Christensen, A. Jackson, and J. Wicht (2000), Core flow inversion tested with numerical dynamo models, *Geophys. J. Int.*, *141*, 485–497, doi:10.1046/j.1365-246x.2000.00097.x.

Roberts, P. H., and G. A. Glatzmaier (2000), A test of the frozen-flux approximation using a new geodynamo model, *Philos. Trans. R. Soc. London, Ser. A*, *358*, 1109–1121, doi:10.1098/rsta.2000.0576.

Roberts, P. H., and S. Scott (1965), On analysis of the secular variation, *J. Geomagn. Geoelectr.*, *17*, 137–151.

Sabaka, T. J., N. Olsen, and M. Purucker (2004), Extending comprehensive models of the Earth's magnetic field with Ørsted and CHAMP data, *Geophys. J. Int.*, *159*, 521–547, doi:10.1111/j.1365-246X.2004.02421.x.

Shure, L., R. L. Parker, and G. Backus (1982), Harmonic splines for geomagnetic modelling, *Phys. Earth Planet. Inter.*, *28*, 215–229, doi:10.1016/0031-9201(82)90003-6.

Takahashi, F., M. Matsushima, and Y. Honkura (2005), Simulations of a quasi-Taylor state geomagnetic field including polarity reversals on the Earth simulator, *Science*, *309*, 459–461, doi:10.1126/science.1111831.

Wardinski, I., and R. Holme (2006), A time-dependent model of the Earth's magnetic field and its secular variation for the period 1980–2000, *J. Geophys. Res.*, *111*, B12101, doi:10.1029/2006JB004401.

Whaler, K. (2007), Core motions, in *Encyclopedia of Geomagnetism and Paleomagnetism*, edited by D. Gubbins and E. Herrero-Bervera, pp. 84–89, Springer, Dordrecht, Netherlands.

A. Chulliat, Equipe de Géomagnétisme, Institut de Physique du Globe de Paris, 4 place Jussieu, F-75005 Paris, France. (chulliat@ipgp.fr)

N. Olsen, DTU Space and Niels Bohr Institute, Juliane Maries Vej 30, DK-2100 Copenhagen, Denmark. (nio@space.dtu.dk)